Korean Journal of Chemical Engineering (2025) 42:1539–1548
https://doi.org/10.1007/s11814-025-00393-5

ORIGINAL ARTICLE

# Effect of Calcination Temperature on the Transformation of Spent NCM811 into Efficient TMO Electrocatalysts

**Hyeeun Kim[1] · Seongkwan Kim[1] · Min-Ho Kim[2] · Chihyun Hwang[3] · Haeseong Jang[1,4]**

Received: 16 November 2024 / Revised: 9 January 2025 / Accepted: 11 January 2025 / Published online: 1 February 2025


## Abstract

The expansion of electric vehicles has increased spent lithium-ion batteries (LIBs) containing valuable transition metals. Recycling these materials reduces economic costs and addresses resource shortages. Additionally, transition metal-based catalysts derived from spent LIBs can replace expensive noble metal catalysts. This study examines the catalytic performance of spent $LiNi_{0.8}Co_{0.1}Mn_{0.1}O_2$ (NCM811) materials, enhanced by adjusting mixed valence states and defect structures. Increasing calcination temperature transformed the layered structure into spinel and rock salt phases, inducing mixed valence states. Consequently, the optimized NCM catalysts exhibited improved catalytic activity in both the oxygen reduction reaction (ORR) and the oxygen evolution reaction (OER). The ORR onset potential increased by 0.07 V, while the OER overpotential decreased by about 26.9%. In a zinc-air battery, the optimized catalyst demonstrated a discharge capacity of 792.1 mAh $g^{-1}$ and stable performance over 100 cycles. *Operando* X-ray absorption spectroscopy (XAS) confirmed Mn as the main active site, with Ni and Co enhancing Mn's activity as electron donors and acceptors. These findings suggest that calcination-induced structural changes and mixed valence states enhance Mn site reactivity, improving catalytic performance. Overall, this study highlights the feasibility of repurposing spent LIB cathode materials into efficient electrocatalysts, thereby improving the economic viability and sustainability of catalyst development.

**Keywords** Spent lithium-ion battery recycling · TMO electrocatalyst · Oxygen reduction reaction · Oxygen evolution reaction

## Introduction

The overconsumption of fossil fuels has resulted in significant environmental challenges, including climate change, air pollution, and energy depletion. In response, global initiatives seek to decrease carbon emissions by 30–40% by 2030, with the ultimate goal of achieving net-zero emissions by 2050. A key strategy in this effort is transitioning to renewable energy technologies, which require efficient and scalable energy storage systems [1–6]. Zinc-air batteries (ZABs) have attracted attention as an energy storage solution because of their high energy density (up to 1086 Wh $kg^{-1}$) and low environmental impact [7]. Compared to lithium-ion batteries (LIBs), ZABs offer a lighter and more environmentally friendly alternative for electric vehicles and other high-energy–density applications. However, the effectiveness of ZABs is impeded by slow oxygen reduction reaction (ORR) kinetics during discharge and the oxygen evolution reaction (OER) kinetics during charge, which reduce their overall efficiency. Overcoming these challenges necessitates the use of efficient electrocatalysts to accelerate ORR and OER kinetics [8–10]. Noble metal catalysts, such as platinum (Pt) and iridium oxides ($IrO_2$), are commonly used because of their superior catalytic performance; however, their high cost and limited durability restrict their widespread use [11, 12].

✉ Chihyun Hwang
winyard22@gmail.com

✉ Haeseong Jang
hjang4765@gmail.com

1 Department of Advanced Materials Engineering, Chung-Ang University, 4726, Seodong-Daero, Daedeok-Myeon, Anseong, Gyeonggi-do 17546, Republic of Korea

2 Chemical and Biomolecular Engineering, University of California, Los Angeles, CA 90095, USA

3 Advanced Batteries Research Center, Korea Electronics Technology Institute, Seongnam, Gyeonggi-do 13509, Republic of Korea

4 Department of Intelligent Energy and Industry, Chung-Ang University, Seoul 06974, Republic of Korea

With the rapid expansion of the LIB market (expected to account for 70% of the battery market by 2025), the increasing demand driven by the growth of electric vehicle and consumer electronics production raises concerns regarding resource depletion, waste generation, and the environmental impact of disposal [13]. The recycling of spent LIBs presents an opportunity to recover valuable materials and address these concerns. Among the materials recovered, nickel (Ni) cobalt (Co) manganese (Mn) (NCM) oxides prove to be a valuable resource for upcycling into electrocatalysts, as they contain transition metals that exhibit mixed valence states (e.g., $Ni^{2+}/Ni^{3+}$, $Co^{2+}/Co^{3+}$, and $Mn^{3+}/Mn^{4+}$). Optimizing these mixed valence states can improve electrocatalytic activity for ORR and OER [14–18].

This study investigates the feasibility of utilizing recycled NCM materials as transition metal oxide (TMO) electrocatalysts for ZABs, focusing on how their structural and electronic properties evolve through cycling and thermal treatments. The recycled cathode materials underwent structural changes, such as reduced particle size and enhanced surface properties, facilitating catalytic performance improvements. Additionally, the effects of different calcination temperatures were analyzed to assess their influence on catalytic performance. As the calcination temperature increased, significant improvements in ORR and OER kinetics were observed owing to phase transitions and the formation of mixed valence states. In particular, 400 °C calcined NCM (A-NCM-400), exhibited superior activity in both reactions. These findings suggest that recycling spent LIB cathode materials can provide an efficient and sustainable solution for next-generation energy storage systems.

## Experiment

### Synthesis of Transition Metal-Based Catalysts

A degradation of NCM811 was conducted in coin cells. The electrodes were prepared by mixing 80 wt% active materials, 10 wt% Super P, and 10 wt% polyvinylidene difluoride binder in N-methyl-2-pyrrolidone (NMP) to form slurries. Subsequently, these slurries were coated onto an aluminum foil using a doctor blade and dried at 100 °C under vacuum for 12 h. The electrodes were punched and assembled into coin cells inside an argon (Ar)-filled glove box. A Li metal foil was used as the anode, and a 1.3 M solution of $LiPF_6$ in a mixture of ethylene carbonate, ethyl methyl carbonate, and dimethyl carbonate (3:4:3) was used as the electrolyte. The coin cells were first cycled in constant current mode (3–4.3 V at 5 C-rate for 100 cycles), after which they were charged to 5 V at 0.1 C-rate and maintained at 5 V until the current decreased to 0.05 C-rate. After cell disassembly, the delithiated electrodes were ultrasonically detached from the aluminum foil using NMP and then separated using centrifugation. The active materials were washed and centrifuged several times with dimethyl carbonate and ultrapure water. Following this cleaning step, the materials were dried thoroughly, after which they underwent thermal treatments at 200 °C, 400 °C, and 600 °C for 3 h using a tube furnace. Based on their treatment, the samples were categorized as cycling before NCM (B-NCM), cycling after NCM (A-NCM), 200 °C calcined NCM (A-NCM-200), 400 °C calcined NCM (A-NCM-400), and 600 °C calcined NCM (A-NCM-600).

### Characterization of Materials

The structural characteristics, including surface cracking and morphological changes, were assessed using field-emission scanning electron microscopy (FE-SEM; HITACHI S-4300). Subsequently, X-ray diffraction (XRD; D/Max2000, Rigaku) was conducted to assess any phase transitions, structural changes, and elemental composition. The local atomic environment, chemical states, and electronic structures of the materials were analyzed using X-ray absorption spectroscopy (XAS) with the Pohang Light Source-II.

### Electrochemical Measurement

Half-cell experiments were performed using three different samples: B-NCM811, A-NCM811, and A-NCM811 calcined at 200 °C, 400 °C, and 600 °C, respectively. A standard three-electrode system was utilized, with Ag/AgCl serving as the reference electrode and a Pt wire as the counter electrode. The electrolyte solution used was a 0.1 M KOH solution. Linear sweep voltammetry (LSV) measurements were recorded at a scan rate of 5 mV $s^{-1}$. For OER measurements, the potential range was 0.1776–0.7776 V against Ag/AgCl and 0.2776–0.9224 V against Ag/AgCl for ORR measurements. The measured LSV curves were corrected for iR drop using the following equation:

$$E = E_{RHE} - i \times R_s \quad (1)$$

To prepare the catalyst ink, 2 mg of B-NCM811, A-NCM811, and A-NCM811 calcined at 200 °C, 400 °C, and 600 °C, respectively, were individually dispersed in a solvent mixture of ethanol and ultrapure water (0.3 mL, with a 2:1 volume ratio of ethanol to water), followed by the addition of 40 µL of 5 wt% Nafion solution. The resulting solution was sonicated for 10 min to achieve homogeneity. The ink was applied onto a glassy carbon (GC) disk electrode with a 4 mm diameter, and a final catalyst loading of 0.25 mg/$cm^2$ was achieved. The electrodes were then dried and used for electrochemical testing.

For the ZAB tests, B-NCM811 and A-NCM811 (calcined at 400 °C) were used as catalysts. To prepare the electrode ink for catalysts, 4 mg of catalyst was mixed with 1 mg of ketjen black (KB) and then dispersed in 500 µL of a 1:1 mixture of isopropyl alcohol (IPA) and ultrapure water, along with 50 µL of 5 wt% Nafion solution. The air electrode was fabricated using this ink. A zinc plate was used as the anode, and the electrolyte consisted of 6 M of KOH and 0.2 M of ZnO. Discharge tests were carried out at a current density of 10 mA $cm^{-2}$, and charge–discharge cycling tests were performed at 5 mA $cm^{-2}$.

## Result and Discussion

### Physical Properties

Figure 1(a) shows a schematic outlining the procedure for recycling and calcining NCM cathode materials from spent LIBs for application as electrocatalysts in ZABs. After 100 cycles and subsequent overcharging to 5 V, the delithiated NCM coin cell was physically disassembled, and the cathode was recovered. Overcharging was conducted to replicate the structural changes and performance degradation that battery electrode materials may experience under actual operating conditions and to extract $Li^+$. DMC and NMP were used to remove the electrolyte and PVDF binder adhered to the cathode material. Subsequently, deionized water was used to eliminate residual impurities, and the recovered powder was dried to obtain A-NCM. The powder was then calcined in a tube furnace under an Ar atmosphere for 3 h at temperatures of 200 °C, 400 °C, and 600 °C, yielding A-NCM-200, A-NCM-400, and A-NCM-600, respectively. These specific temperatures were selected to evaluate the diverse structural characteristics of NCM, including its layered structure, spinel structure, and rock salt structure, as well as their corresponding effects on material performance. During repeated charge–discharge cycles, the cathode material in

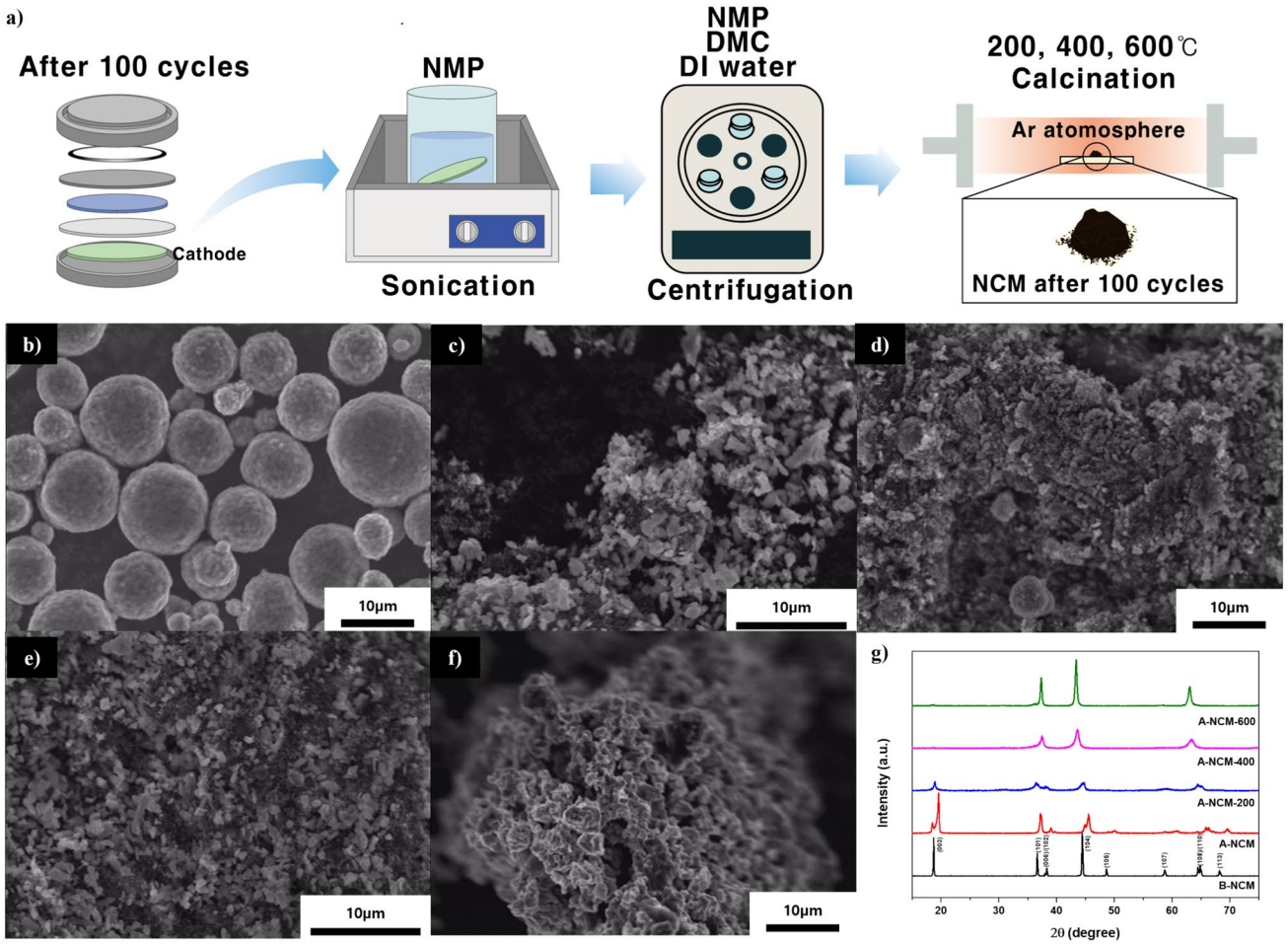


**Fig. 1** **a** Schematic of the recycling process of the cathode active materials in spent LIBs as an electrocatalyst for a ZAB. SEM images of **b** B-NCM, **c** A-NCM, **d** A-NCM-200, **e** A-NCM-400, and **f** A-NCM-600. **g** XRD patterns of B-NCM, A-NCM, A-NCM-200, A-NCM-400 and A-NCM-600

spent LIBs deteriorates because of structural collapse caused by lithium-ion insertion/extraction and lattice oxygen evolution [19]. SEM was conducted to analyze the morphology and structural changes. Figure 1(b) shows the B-NCM sample, characterized by the formation of spherical secondary particles resulting from the aggregation of primary particles measuring tens to hundreds of nanometers [20]. After cycling, A-NCM exhibited particle size decline and cracks owing to repeated $Li^+$ insertion/extraction and high voltage charge–discharge conditions (> 4.0 V, Li/$Li^+$) (Fig. 1(c)). These processes induce anisotropic volume changes, internal stress between primary particles, and phase transitions in Ni-rich NCM, ultimately leading to the fractured morphology observed in A-NCM [21–23]. As shown in Fig. 1(d–f), a porous structure emerged, accompanied by particle recrystallization, as the calcination temperature increased (200 °C, 400 °C, 600 °C) [24]. XRD was performed to investigate the structural evolution of A-NCM and its thermally treated variants (A-NCM-200, A-NCM-400, and A-NCM-600) (Fig. 1(g)). The XRD pattern of B-NCM confirms the presence of a typical α-$NaFeO_2$ layered structure, with sharp peaks representing well-ordered crystalline phases [25, 26]. The observed peak broadening in A-NCM compared to B-NCM indicates a reduction in average crystal particle size, as predicted by the Scherrer equation. This reduction in crystallite size after cycling is attributed to the structural disorder and decomposition of the layered structure during thermal treatment [27]. Upon calcination at 200 °C, the (105) and (113) peaks disappeared, and a new peak at 31.2° appeared, corresponding to the (220) plane of the spinel structure. This indicates a phase transition from a layered structure to a spinel phase due to delithiation and thermal treatment. At 400 °C, the XRD peaks shifted, revealing diffraction peaks at 37.5°, 43.6°, and 63.3°, corresponding to the (111), (200), and (220) planes of the rock salt structure, respectively. This shift signifies the evolution from a spinel to a rock salt structure, influenced by increased cation disorder and structural rearrangement during calcination at elevated temperatures. In the case of A-NCM-600, the XRD peaks show a marked increase in intensity compared to A-NCM-400, indicating that the phase transition to the rock salt structure progressed further, with greater crystallinity at elevated temperatures. These XRD and SEM results demonstrate that the NCM undergoes a reduction in particle size after cycling as well as a progressive phase transition from a layered structure to a spinel and ultimately to a rock salt structure during calcination.

X-ray absorption near-edge structure (XANES) analysis was conducted to examine the electronic structure changes. The pre-edge peaks observed in the XANES spectra correspond to transitions of 1 s core electrons to 3d orbitals [28]. As shown in the inset of Fig. 2(a–c), the pre-edge intensities at the Ni, Co, and Mn K-edges initially increased upon calcination (up to 200 °C), indicating enhanced 3d-4p orbital hybridization due to local structural distortions [29]. However, as the temperature increased to 600 °C, the intensities decreased, indicating a structural transition toward a more centrosymmetric configuration and reduced hybridization [30]. These observations across the Ni, Co, and Mn K-edges in the insets of Fig. 2(a–c) indicate a unified structural evolution during thermal treatment, where early distortions enhanced hybridization, but subsequent phase transitions reduced it at elevated temperatures. The shift in the white line position of the Ni, Co, and Mn K-edges indicates changes in their oxidation states. In the XANES spectra of A-NCM, the white line exhibited a blue shift, in contrast to B-NCM, indicating an increase in the oxidation states of Ni, Co, and Mn after cycling. As shown in Fig. 2(a), the white line of A-NCM was positioned at a higher energy level than that of $Ni_2O_3$, suggesting the presence of $Ni^{4+}$. As the calcination temperature of A-NCM increased, a red shift in the white line was observed, indicating a gradual reduction of Ni from $Ni^{4+}$ to $Ni^{3+}$ and $Ni^{2+}$. Similarly, in Fig. 2(b), the white line of A-NCM was at a higher energy level than that of $Co_3O_4$, indicating the presence of $Co^{4+}$. A red shift in the white line with increasing calcination temperature indicates the reduction of Co from $Co^{4+}$ to $Co^{3+}$ and $Co^{2+}$. In Fig. 2(c), the white line of A-NCM was at a higher energy level than that of $MnO_2$, indicating that Mn exists in a higher oxidation state than $Mn^{4+}$. As the calcination temperature increased, a red shift in the white line was observed, indicating the reduction of Mn. The XANES spectra of the Ni, Co, and Mn K-edges in Fig. 2(a–c) revealed that the transition metals were oxidized after cycling in B-NCM and reduced as the calcination temperature increased in A-NCM. This suggests the presence of mixed valence states in calcined A-NCM. The shift in photon energy of the white line from A-NCM to A-NCM-600 was measured at 4.6 eV for Ni, 2.8 eV for Co, and 1.9 eV for Mn, indicating that Ni is the most thermally unstable element, while Mn is the most thermally stable. Linear combination fitting (LCF) of the Ni, Co, and Mn K-edges in Fig. 2(d–f) was performed to quantitatively analyze the relative phase proportions within the material. Ni and Co exhibited phase transitions from a layered structure to spinel and rock salt structures as the calcination temperature increased, while Mn primarily transitioned from a layered to spinel structure. These findings are consistent with the XRD results, which indicate transitions in structures from layered to spinel and rock salt structures. Figure 2(g–i) shows the $k^3$-weighted Ni, Co, and Mn K-edge extended X-ray absorption fine structure (EXAFS) spectra, which were analyzed to access local structural changes after cycling and calcination. Each spectrum displayed two distinct peaks: the first peak corresponds to TM—O (TM = Ni,

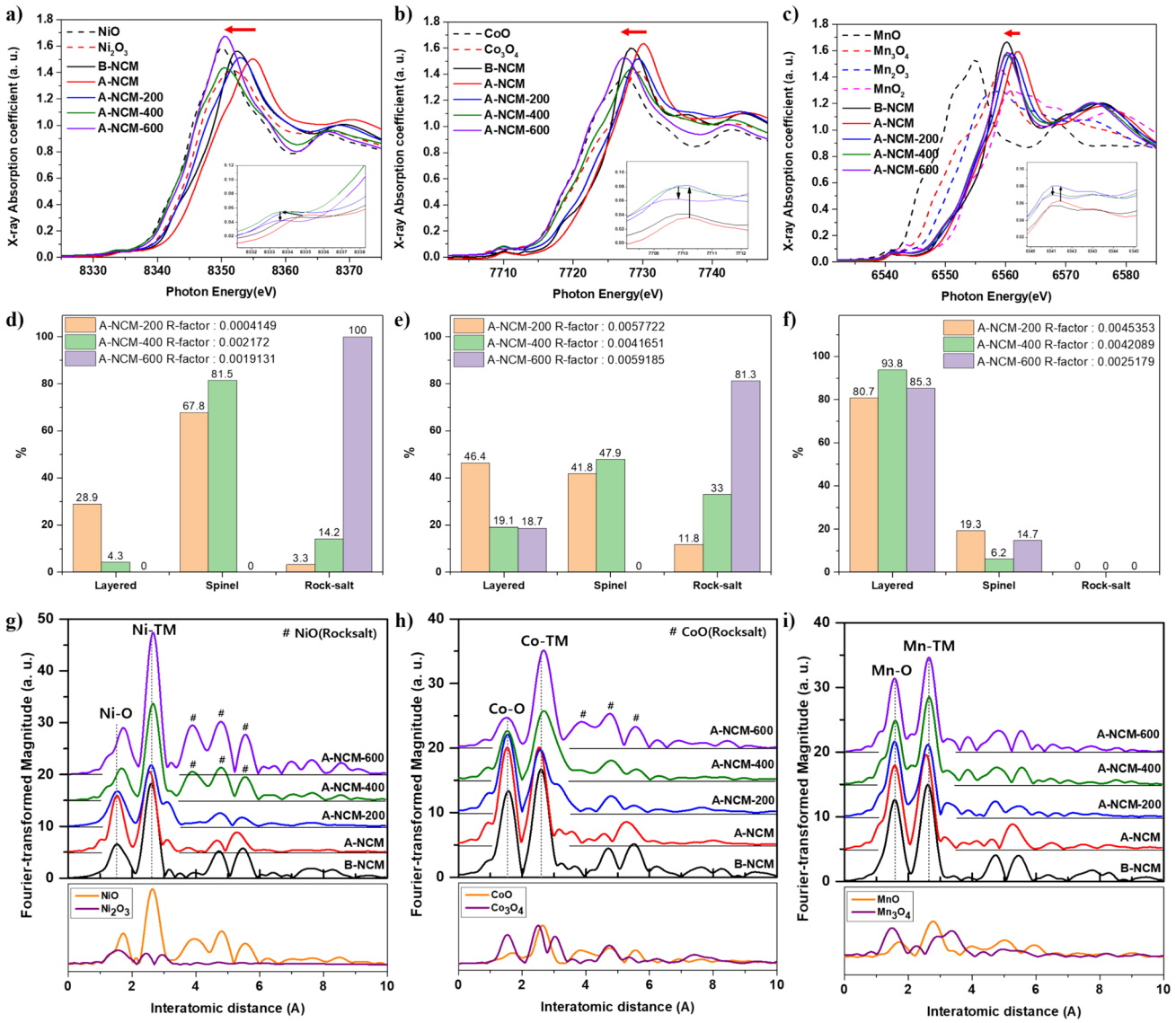


**Fig. 2** XANES of NCM; **a** Ni K-edge, **b** Co K-edge, and **c** Mn K-edge. LCF of NCM; **d** Ni K-edge, **e** Co K-edge, and **f** Mn K-edge. Comparison of the **g** Ni, **h** Co, and **i** Mn K-edge Fourier transform magnitudes of $k^3$-weighted EXAFS spectra of NCM. The spectra shown below are reference spectra for corresponding TM oxide

Co, and Mn) bond interactions, while the second corresponds to TM—TM interactions. The x-axis of these peaks represents the bond length, with the peak intensity reflecting the coordination number. In Fig. 2(g), the Ni—O bond length remained constant at 1.534 Å for both A-NCM and A-NCM-200; however, the intensity of the Ni—O peak decreased in A-NCM-200, indicating a weakening of the Ni—O bond and an increase in oxygen vacancies [31]. At 400 °C and 600 °C, the Ni—O bond length increased to 1.687 Å and 1.718 Å, respectively, while the intensity of the Ni—TM peak increased. Additionally, the appearance of peaks corresponding to the rock salt phase (denoted by "#") indicates a transition from a spinel to a more ordered rock salt structure at elevated temperatures. In Fig. 2(h), the Co—O bond length decreased from 1.565 Å to 1.503 Å, followed by a decrease in peak intensity with elevated calcination temperatures. The appearance of peaks associated with CoO in the rock salt structure was also observed at 600 °C. In Fig. 2(i), the Mn—O bond length remained stable at 1.595 Å from A-NCM to A-NCM-400; however, a decline in the Mn—O peak intensity occurred, suggesting an increase in oxygen vacancies around Mn during the calcination process. XAS analysis revealed the changes in electronic properties and local structure during

calcination, including the formation of mixed valence states, phase transitions, and oxygen vacancies.

## Electrochemical Properties

LSV tests were conducted in alkaline media using a rotating ring-disk electrode to examine the catalytic activities of the electrocatalysts during the ORR and OER. Initially, KB was not added to the samples to observe the trends in TMOs. The OER and ORR performances of B-NCM, A-NCM, and calcined A-NCM were evaluated in a standard three-electrode setup with a rotating disk electrode (1600 rpm) in $O_2$-saturated 0.1 M KOH. Figure 3(a) displays the OER LSV curves with iR compensation. The onset potential of A-NCM was reduced by 0.1 V, from 1.79 V for B-NCM to 1.69 V. The onset potential of A-NCM-200 was observed to be 1.67 V, surpassing the values obtained for A-NCM-400 (1.68 V), A-NCM-600 (1.73 V), and bare GC (1.79 V). In Fig. 3(b), the OER overpotentials at 10 mA $cm^{-2}$ are compared, with A-NCM showing a lower overpotential (546 mV) than B-NCM (689 mV); this indicates enhanced OER activity after cycling. The calcined samples A-NCM-200 and A-NCM-400 exhibited even lower overpotentials of 504 mV and 541 mV, respectively. The Tafel slope analysis (Fig. 3(c)) revealed that A-NCM-200 had a Tafel slope of 75.8 mV $dec^{-1}$, which was superior to that of $RuO_2$. This difference suggests relatively fast rate-determining step kinetics. Figure 3(d) shows the ORR polarization curves, where A-NCM calcined at 400 °C exhibited the highest half-wave potential (0.711 V), indicating improved ORR performance compared to B-NCM (0.642 V) after charge–discharge cycling and calcination. Figure 3(e) compares the ORR onset potentials, with A-NCM-400 showing the highest onset potential of 0.835 V, outperforming B-NCM (0.765 V), A-NCM (0.783 V), A-NCM-200 (0.788 V), A-NCM-600 (0.784 V), and bare GC (0.744 V). Figure 3(f) presents the ORR Tafel slopes, where A-NCM-400 exhibited the optimal kinetics, with a Tafel slope of 93.9 mV $dec^{-1}$, outperforming the other NCM samples. Compared to B-NCM, A-NCM exhibited enhanced OER and ORR performance. This improvement is attributed to the increased surface area and enhanced electron transport, both resulting from repeated lithium insertion and extraction during cycling [32]. The OER performance of the A-NCM calcined samples was highest at 200 °C, followed by 400 °C and 600 °C. In contrast, the ORR performance was optimal at 400 °C, followed by 200 °C and 600 °C. To address the low conductivity in practical applications, A-NCM-400 was tested with KB through physical mixing. The results of these tests are shown in Fig. S1.

To analyze the effects of mixed valence states, phase transitions, and oxygen bonding induced by cycling and thermal treatments on the catalytic activity of recycled NCM 811-based electrocatalysts, *operando* XAS analysis was conducted. The cyclic voltammetry profiles recorded during *operando* XAS measurements are presented in Fig. S2.

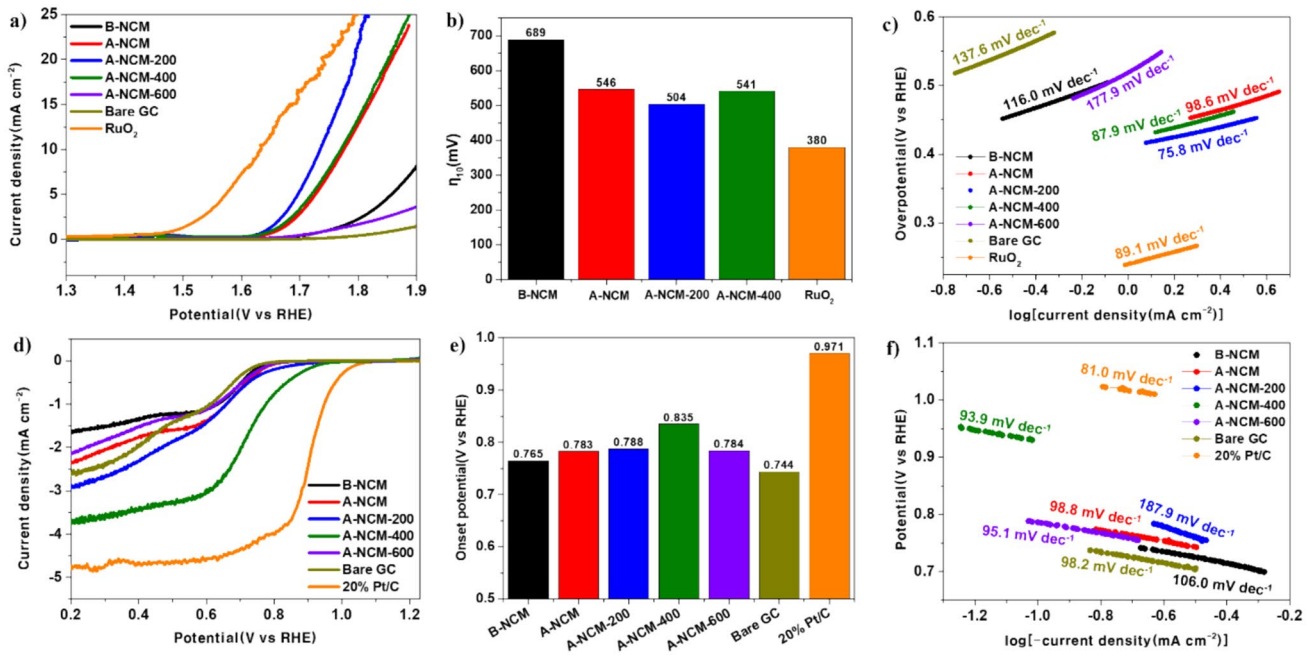


**Fig. 3** **a** OER polarization curves of B-NCM, A-NCM, A-NCM-200, A-NCM-400, A-NCM-600, bare GC, and $RuO_2$. **b** Comparison of OER overpotential at 10 mA $cm^{-2}$. **c** Tafel slopes of OER; **d** ORR polarization curves of B-NCM, A-NCM, A-NCM-200, A-NCM-400, A-NCM-600, Bare GC, and 20% Pt/C; **e** Comparison of ORR onset potential. **f** Tafel slopes of ORR

The scan ranges for the various reactions were as follows: ORR1 was conducted from 1.00 to 0.23 V, ORR2 from 0.23 to 1.00 V, OER1 from 1.00 to 1.53 V, and OER2 from 1.53 to 1.00 V (V vs. RHE). The scan rate for these measurements was set at 0.085 mV $s^{-1}$. Figure 4(a–c) presents the Ni, Co, and Mn K-edge XANES spectra. In the XANES spectra, an X-ray absorption coefficient of 0.5 was observed, corresponding to the adsorption edge [33], and the changes in photon energy at this point were indicative of variations in oxidation states. Figure 4(g) shows the photon energy changes at an X-ray absorption coefficient of 0.5 for Ni, Co, and Mn K-edges during the ORR and OER. A decrease in ΔPhoton energy indicates a decrease in the oxidation state, while an increase in ΔPhoton energy indicates an increase in the oxidation state. Notably, Mn exhibited a more significant reduction in intensity compared to Ni and Co, suggesting its greater involvement in oxygen catalysis. The decrease in ΔPhoton energy observed for Mn during ORR indicates its role as an active site for the adsorption and desorption of oxygen intermediates; the fluctuation in ΔPhoton energy reflects the dynamic nature of these intermediates as they undergo adsorption and desorption processes. During OER, a pronounced reduction in ΔPhoton energy was observed; this is attributable to the interaction of Mn with electron-dense hydroxyl ($OH^-$) species. These results highlight the role of Mn as an active site during both ORR and OER.

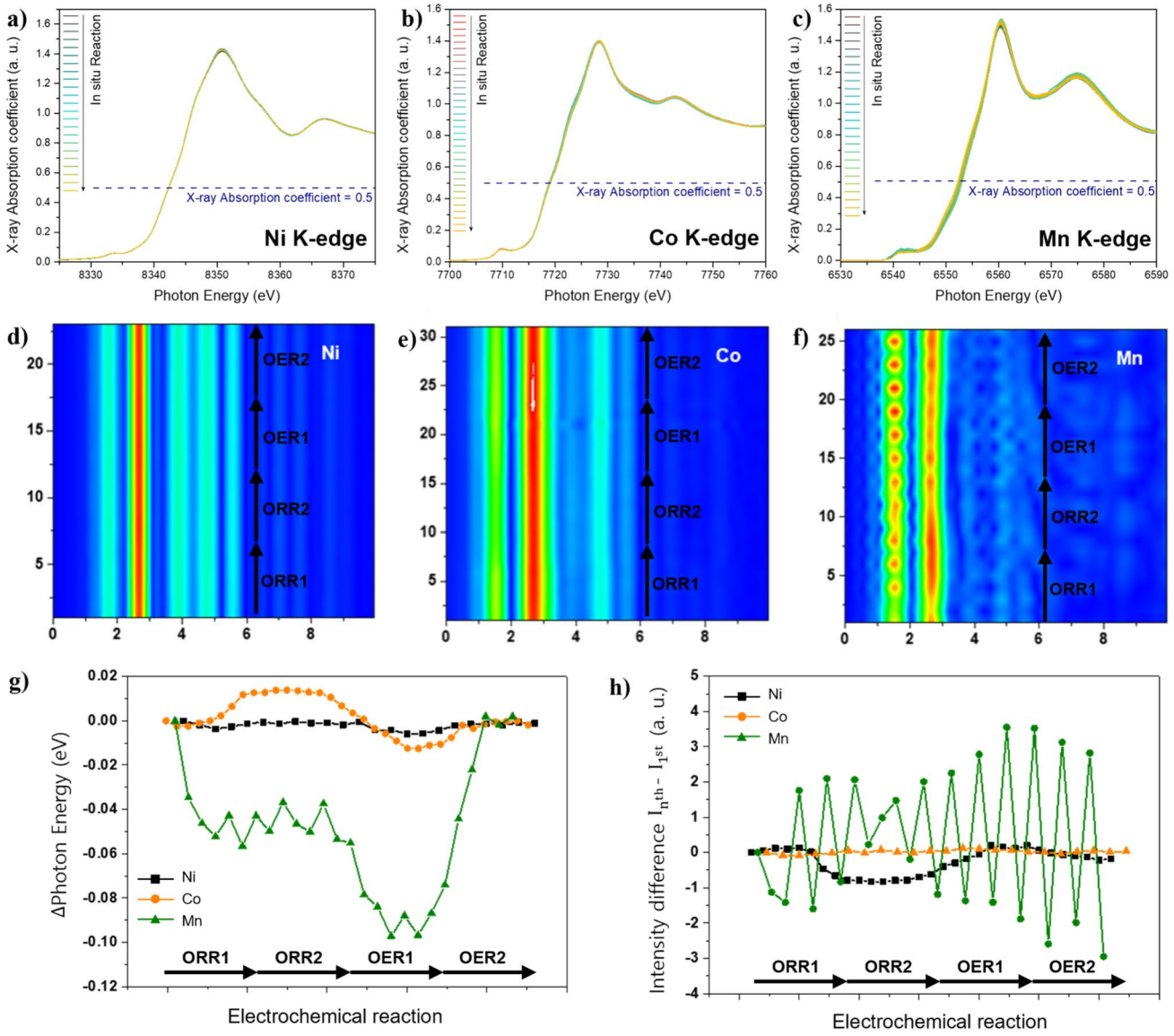


**Fig. 4** *Operando* XANES for A-NCM-400 at **a** Ni K-edge, **b** Co K-edge, and **c** Mn K-edge. Contour maps displaying *operando* $k^3$-weighted EXAFS at **d** Ni K-edge, **e** Co K-edge, and **f** Mn K-edge. **g** Photon energy changes at an X-ray absorption coefficient of 0.5 observed in *operando* XANES. **h** Intensity changes of the TM-O peak in *operando* $k^3$-weighted EXAFS

Conversely, Co underwent smaller changes in oxidation state compared to Mn. In the ORR, Co supplies the required electrons for oxygen electrocatalysis, leading to a reduction in its oxidation state, while during OER, Co stabilizes Mn by acquiring electrons, rather than directly interacting with $OH^-$ species. This highlights the role of Co as an electron donor/acceptor, specifically in supporting Mn during OER. Ni exhibited minimal changes in photon energy, indicating its function as a structural component rather than an active site. While Ni may support Co as a secondary electron donor/acceptor, its involvement in oxygen intermediate reactions is more limited than that of Mn and Co. Figure S3 presents the *operando* $k^3$-weighted EXAFS profiles, which revealed TM-O scattering peaks at around 1.73 Å, 1.52 Å, and 1.53 Å, characteristic of metal oxides. Figure 4(d–f) and Fig. S4 show the contour maps of the *operando* $k^3$-weighted EXAFS spectra at the Ni, Co, and Mn K-edges. Mn exhibited substantial variability in TM-O bond length during the ORR and OER, while Ni and Co showed minimal changes, further confirming that Mn was the primary active site. Figure 4(h) shows the changes in TM-O peak intensity ($\Delta I$: $I_{nth} - I_{1st}$) during electrochemical reactions, reflecting changes in coordination number. Ni and Co experienced smaller changes in TM-O peak intensity than Mn, which underwent repeated increases and decreases, confirming its role as the key site for intermediate adsorption and desorption. In conclusion, the *operando* XAS analysis revealed that Mn is the primary active site in A-NCM-400 during both ORR and OER, with Co acting as the support electron donor/acceptor and Ni functioning as a secondary stabilizer during electron transfer. The *operando* XAS analysis results provide insights into the performance differences observed at different calcination temperatures during the ORR and OER. Based on the above results, the mechanism responsible for the improvement in activity of the calcined NCM catalyst can be speculated as follows. At 400 °C, the formation of a mixed-metal spinel structure becomes predominant, and the mixed-valence states of $Ni^{2+}/Ni^{3+}$ and $Co^{2+}/Co^{3+}$ facilitate electron transfer to Mn [34, 35]. This enhanced electron mobility reduces the overpotential required for oxygen reduction and results in improved ORR activity [36]. Conversely, during the OER, A-NCM-200 exhibits excellent activity, primarily due to the presence of increased oxidation states of Ni and Co ($Ni^{4+}$ and $Co^{4+}$) compared to the 400 °C sample. The high-valence $Ni^{4+}$ and $Co^{4+}$ ions, being unstable, are more likely to accept electrons [37, 38], thereby acting as efficient electron acceptors during the OER. This leads to a faster electron withdrawal from the oxygen species, thereby enhancing the OER kinetics and resulting in higher activity at 200 °C. At 600 °C, Ni and Co formed a predominant rock salt structure, which, due to its more ordered nature, results in reduced electron mobility [39]. The stabilized $Ni^{2+}$ and $Co^{2+}$ ions in this structure were less effective as electron donors or acceptors [40], significantly hampering both ORR and OER performance.

ZAB tests were conducted to investigate the practical utility of A-NCM-400. A-NCM-400 outperformed B-NCM in terms of OER and ORR performance during half-cell electrochemical tests. As seen in Fig. 5(a), A-NCM-400 showed a higher power density of 152.16 mW $cm^{-2}$ compared to that of B-NCM (118.23 mW $cm^{-2}$). As shown in Fig. 5(b), the discharge capacity of the A-NCM-400-based ZAB was 792.1 mAh $g^{-1}$, outperforming the B-NCM-based ZAB (730.0 mAh $g^{-1}$). Moreover, Fig. 5(c) shows that A-NCM-400 demonstrated superior stability over 100 cycles compared to B-NCM. These test results are consistent with previous results, where A-NCM-400 demonstrated superior OER and ORR catalytic activity compared to B-NCM, demonstrating that this enhanced catalytic performance is reflected in the improved battery performance, further highlighting the potential of A-NCM-400 as a durable air cathode for aqueous rechargeable ZABs.

## Conclusion

In this study, the feasibility of converting spent NCM811 into efficient TMO electrocatalysts for ZABs through cycling and thermal treatments was investigated. Structural and electronic changes were analyzed using SEM, XRD, *Ex-situ* XAS, and *operando* XAS. Cycling resulted in microcracks and reduced particle size, thereby increasing the surface area. Thermal treatments at 200 °C, 400 °C, and 600 °C caused phase transitions from layered to spinel and rock salt structures. *Ex-situ* XAS confirmed these transitions and revealed mixed valence states and oxygen vacancies due to transition metal reduction during calcination. *Operando* XAS provided mechanistic insights, identifying Mn as the primary active site for OER and ORR, with Co and Ni acting as electron donors/acceptors to facilitate these processes at the Mn site. A-NCM-200 showed optimal OER activity due to the presence of high-valence $Ni^{4+}$ and $Co^{4+}$, which effectively acted as electron acceptors. A-NCM-400 exhibited optimal ORR performance due to the presence of mixed-valence states of $Ni^{2+}/Ni^{3+}$ and $Co^{2+}/Co^{3+}$ within the spinel structure, which facilitated electron transfer to Mn In contrast, the ordered rock salt structure of Ni and Co in A-NCM-600 led to decreased catalytic activity in both OER and ORR, attributed to its limited electron mobility. During ZAB tests, A-NCM-400 achieved a power density of 152.16 mW $cm^{-2}$ and a discharge capacity of 792.1 mAh $g^{-1}$, outperforming B-NCM. This underscores its potential as an effective TMO electrocatalyst. In summary, this study demonstrates the feasibility of transforming recycled NCM811

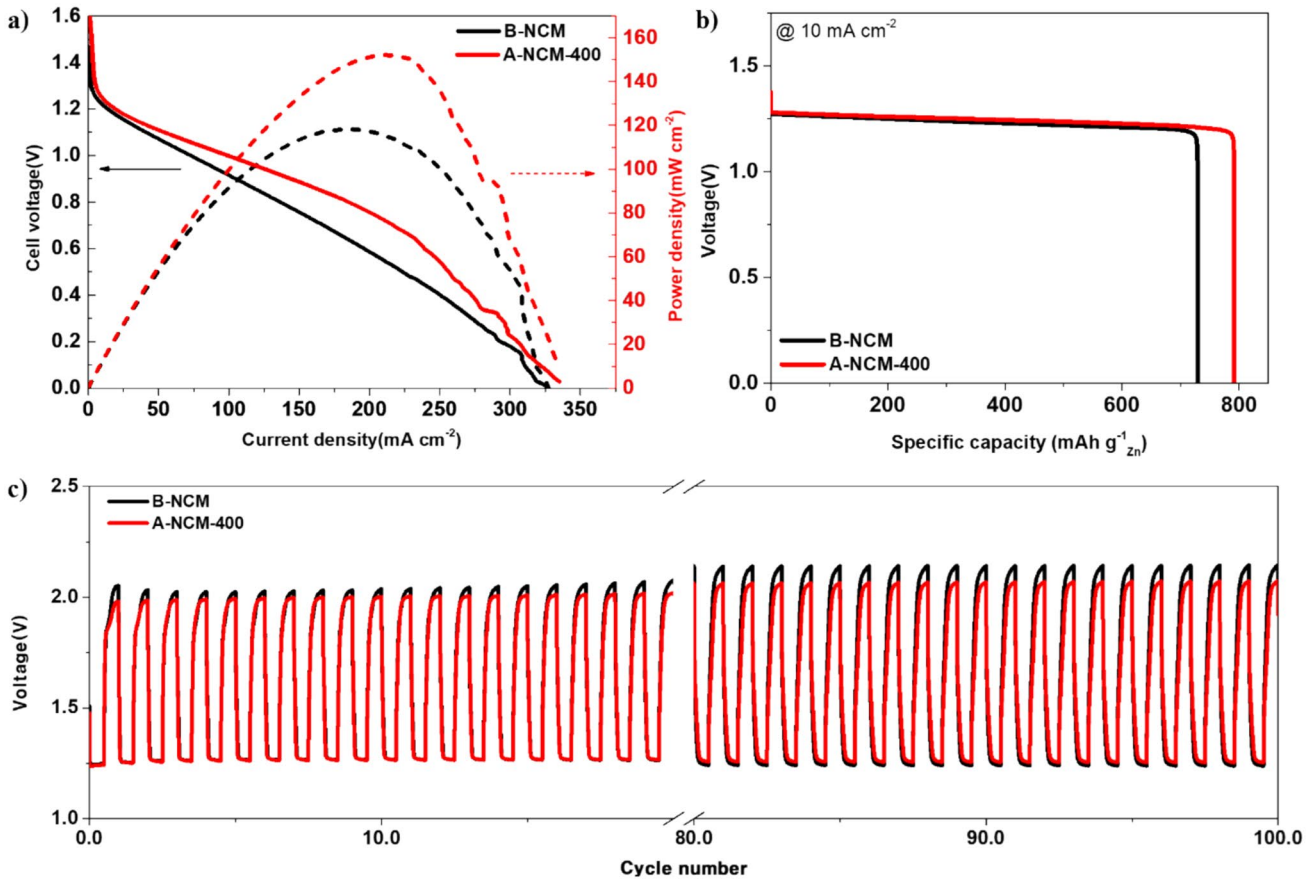


**Fig. 5** **a** Discharge polarization and power density curves; **b** discharge profiles of ZABs at 10 mA $cm^{-2}$; and **c** long-term cycling performance at a current density of 5 mA $cm^{-2}$ using B-NCM and A-NCM-400 as air cathodes

into sustainable high-performance TMO electrocatalysts for next-generation energy storage systems, with A-NCM-400 offering the best balance of catalytic activity.

**Supplementary Information** The online version contains supplementary material available at https://doi.org/10.1007/s11814-025-00393-5.

**Acknowledgements** This research was supported by the Chung-Ang University Research Grants in 2023 and Advancing the Technologies for Scientific Crime Investigation Program through the Korea Institutes of Police Technology(KIPoT) funded by the Korean National Police Agency (RS-2024-00468545).

**Funding** Open Access funding enabled and organized by Chung-Ang University.

**Data availability** All data generated or analyzed during this study are available from the corresponding author upon reasonable request.



## References

1. B.G. Pollet, I. Staffell, J.L. Shang, Electrochim. Acta **84**, 235–249 (2012)
2. Z.Y. Yu et al., Adv. Mater. **33**, 2007100 (2021)
3. S. Chu, A. Majumdar, Nature **488**, 294–303 (2012)
4. C.F. Shih, T. Zhang, J. Li, C. Bai, Joule **2**, 1925–1949 (2018)
5. E.E. Benson, C.P. Kubiak, A.J. Sathrum, J.M. Smieja, Chem. Soc. Rev. **38**, 89–99 (2009)
6. H. Yang et al., Adv. Funct. Mater. **31**, 2007602 (2021)
7. Z. Song et al., Adv. Mater. **32**, 1908127 (2020)
8. F. Cheng, J. Chen, Chem. Soc. Rev. **41**, 2172–2192 (2012)
9. D. Zhao et al., Chem. Soc. Rev. **49**, 2215–2264 (2020)
10. S. Dresp et al., Energy Environ. Sci. **9**, 2020–2024 (2016)
11. Y. Bing, H. Liu, L. Zhang, D. Ghosh, J. Zhang, Chem. Soc. Rev. **39**, 2184–2202 (2010)
12. E.A. Paoli et al., Chem. Sci. **6**, 190–196 (2015)

13. Desjardins, J. Explaining the Surging Demand for Lithium-Ion Batteries, http://www.visualcapitalist.com/explaining-surging-demand-lithium-ion-batteries/ (2016)
14. R. Huang et al., J. Power. Sources **515**, 230640 (2021)
15. K. Amini, J. Gostick, M.D. Pritzker, Adv. Funct. Mater. **30**, 1910564 (2020)
16. J. Park, H. Jin, M. Kim, H. Jang, M. Ko, J. Mater. Chem. A **10**, 18626–18635 (2022)
17. M. Labbe, D.G. Ivey, J. Phys, Energy **6**, 032002 (2024)
18. T. Maiyalagan, K.A. Jarvis, S. Therese, P.J. Ferreira, A. Manthiram, Nature Commun. **5**, 3949 (2014)
19. C. Sun et al., ACS Nano **14**, 6181–6190 (2020)
20. X. Deng et al., Energy Environ. Mater. **6**, e12331 (2023)
21. H.-H. Ryu, K.-J. Park, C.S. Yoon, Y.-K. Sun, Chem. Mater. **30**, 1155–1163 (2018)
22. C. Liang et al., J. Phys. Chem. C **120**, 6383–6393 (2016)
23. J. Li et al., J. Electrochem. Soc. **164**, A655 (2017)
24. T. Priamushko et al., ACS Appl. Energy Mater. **3**, 5597–5609 (2020)
25. L. Ni et al., Adv. Energy Mater. **12**, 2103757 (2022)
26. J.-H. Kim, K.-J. Park, S.J. Kim, C.S. Yoon, Y.-K. Sun, J. Mater. Chem. A **7**, 2694–2701 (2019)
27. S. Britto, S. Joseph, P. Vishnu Kamath, J. Chem. Sci. **122**, 751–756 (2010)
28. X. Liu et al., J. Am. Chem. Soc. **142**, 19745–19753 (2020)
29. K.W. Nam et al., Adv. Funct. Mater. **23**, 1047–1063 (2013)
30. T. Yamamoto, X-Ray Spectrom. **37**, 572–584 (2008)
31. E. Lee et al., Adv. Sci. **7**, 1902413 (2020)
32. J. Zhou et al., Nature Commun. **11**, 1984 (2020)
33. A. Zabilska et al., JACS Au **2**, 762–776 (2022)
34. H. Yuan et al., ACS Appl. Mater. Interfaces **10**, 16410–16417 (2018)
35. Y. Zhou et al., Adv. Mater. **30**, 1705407 (2018)
36. R.J. Toh, A.Y.S. Eng, Z. Sofer, D. Sedmidubsky, M. Pumera, ChemElectroChem **2**, 982–987 (2015)
37. Y.-N. Zhou, F.-T. Li, B. Dong, Y.-M. Chai, Energy Environ. Sci. **17**, 1468–1481 (2024)
38. Q. Wu et al., Nat. Commun. **14**, 997 (2023)
39. Y.-Z. Jin et al., Adv. Energy Mater. **8**, 1703469 (2018)
40. X. Wang et al., Angewandte Chemie International Edition n/a, e202416274.